

**Iván Monge-Concepción**

Department of Mechanical Engineering,  
The Pennsylvania State University,  
University Park, PA 16802  
e-mail: izm4@psu.edu

**Shawn Siroka**

Department of Mechanical Engineering,  
The Pennsylvania State University,  
University Park, PA 16802  
e-mail: sis5702@psu.edu

**Reid A. Berdanier**

Mem. ASME  
Department of Mechanical Engineering,  
The Pennsylvania State University,  
University Park, PA 16802  
e-mail: rberdanier@psu.edu

**Michael D. Barringer<sup>1</sup>**

Mem. ASME  
Department of Mechanical Engineering,  
The Pennsylvania State University,  
University Park, PA 16802  
e-mail: mbarringer@psu.edu

**Karen A. Thole**

Fellow ASME  
Department of Mechanical Engineering,  
The Pennsylvania State University,  
University Park, PA 16802  
e-mail: kthole@psu.edu

**Christopher Robak**

Pratt & Whitney,  
East Hartford, CT 06118  
e-mail: christopher.robak@prattwhitney.com

# Influence of Vane Trailing Edge Flow on the Formation of Cavity Cells and Rim Sealing

*Hot gas ingestion into the turbine rim seal cavity is an important concern for engine designers. To prevent ingestion, rim seals use high-pressure purge flow; however, the penalty is that excessive use of the purge flow decreases engine thermal efficiency. In this paper, a one-stage turbine operating at engine-representative conditions was used to study the effect of steady and time-resolved under-platform cavity temperatures and pressures across a range of coolant flowrates in the presence of vane trailing edge (VTE) flow. This study correlates time-resolved pressure with time-resolved temperature to identify primary frequencies driving ingestion. At certain flowrates, the time-resolved pressures are out of phase with the temperatures, indicating ingestion. Measurements from high-frequency response pressure sensors in the rim seal and vane platform were also used to determine rotational speed and quantity of large-scale structures (cells). In a parallel effort, a computational model using Unsteady Reynolds-averaged Navier–Stokes (URANS) was applied to determine swirl ratio in the rim seal cavity and time-resolved rim sealing effectiveness. The experimental results confirm that at low purge flowrates, the VTE flow influences the unsteady flow field by decreasing pressure unsteadiness in the rim seal cavity. Results show an increase in purge flow increases the number of unsteady large-scale structures in the rim seal and decreases their rotational speed. However, VTE flow was shown to not significantly change the cell speed and count in the rim seal. Simulations point to the importance of the large-scale cell structures in influencing rim sealing unsteadiness, which is not captured in current rim sealing predictive models.*  
[DOI: 10.1115/1.4054281]

**Keywords:** cavity and leaking flows, fluid dynamics and heat transfer phenomena in compressor and turbine components of gas turbine engines

## Introduction

As lofty goals are targeted by the aviation industry to reduce emissions [1], greater efficiency is required for gas turbine engines. One of the driving factors of efficiency is the turbine entry temperature. For several decades, this parameter has surpassed the softening temperature of the turbine components [2] creating durability challenges in the downstream parts.

One area particularly affected by the harsh environment is the turbine cavity region between rotating and stationary components. This region is designed to seal the unprotected wheel space from hot gas path ingestion. Although many types of seals exist, most aviation engines discourage ingress through a combination of various axial and radial clearance changes. The outermost seal where the platform of the blade and platform of the vane overlap is often referred to as the rim seal. Rim seals are subject to ingestion because of their proximity to the main gas path. For that reason, measurements in the rim seal are the main focus of this paper. Secondary air from the compressor is injected at a low radius to pressurize the cavity. Because this bleed air causes a penalty to the efficiency of the engine, it is imperative to develop an

understanding of the physical mechanisms that drive the ingestion and ensure the effective use of secondary air.

Attempts to understand and predict the sealing effectiveness of first-stage turbine cavities through computational modeling are powerful, yet limited. Because this region is a low-potential three-dimensional flow field with time-varying vane–blade interactions, models are either computationally expensive or oversimplified. Under certain flow conditions where fluidic instabilities can develop, such models often result in inaccurate predictions [3,4] because instabilities can create large-scale rotating pressure cells responsible for increased ingestion. As a result, there is a need for time-resolved measurements to develop time-accurate models and understand how to control and manage these flow behaviors.

This paper uses a one-stage turbine with engine-representative hardware and seal geometries to provide a time-resolved dataset linking pressure and temperature events to the steady cooling effectiveness in the rim seal cavity and supplements experimental data with a computational (URANS) model. First, the impact of vane trailing edge (VTE) flow on steady cavity performance is analyzed. Then, the time-resolved pressure and temperature are correlated indicating a connection between coolant flowrates and time-varying ingress. This connection between time-varying pressure and temperature is then related to the cavity sealing performance, indicating the presence of instability in certain flow conditions. Finally, quantification of the instability cell structures is presented in terms of the speed and number of cells over a range of flow conditions.

This article recapitulates the main findings from two previously published works [5,6]. Further information on the correlation

<sup>1</sup>Corresponding author.

Contributed by the International Gas Turbine Institute (IGTI) of ASME for publication in the JOURNAL OF TURBOMACHINERY. Manuscript received December 6, 2021; final manuscript received April 4, 2022; published online May 10, 2022. Assoc. Editor: Vittorio Michelassi.

methods of the time-resolved pressure and temperature signals to cavity performance with an emphasis on the advantages of including a fast-response thermal sensor is presented in Siroka et al. [5] whereas the work by Monge-Concepción et al. [6] provides an in-depth quantification of the rotating cell structures tied to cavity instabilities. The combination of these two separate works enables the explicit connection of physical mechanisms driving fluidic instabilities in the cavity region.

## Literature Review

Hot gas ingestion into the rim seal between stationary and rotating turbine components has been studied experimentally and computationally over the past several decades, as reviewed by Johnson et al. [7] and Scobie et al. [8]. In general, two primary flow mechanisms contribute to the ingestion process including rotation-induced ingestion caused by disk pumping, and pressure-induced ingestion caused by the vane and blade potential fields. Pressure asymmetries due to the presence of the vanes and blades result in alternating regions of high and low pressure in the main gas path annulus. In these alternating pressure patterns, regions of relatively high pressure promote ingestion into the rim seal cavity, and regions of low pressure promote egress from the rim seal cavity.

The majority of the literature on rim seal ingestion includes time-averaged studies that quantify rim sealing effectiveness for varying levels of high-pressure sealing flow injected into the wheelspace cavity. Gradually, ingestion models have been developed based on experimental studies conducted by various research groups. One such model proposes rim sealing predictions through a two-orifice model including one for flow egress and one for flow ingress. Although this model has been successfully implemented, there are conditions where the rim sealing effectiveness data trends deviate from such a model, for example, an inflection region in the rim sealing effectiveness curve observed in previous studies [9–12]. Based on the results by Horwood et al. [13] who evaluated sealing effectiveness with and without blades present, they found that the ingress of highly swirled flow from the main annulus resulted in unstable shear layers between flow in the main annulus and flow in the rim seal. However, the presence of blades promoted the formation of an inflection region in the rim sealing effectiveness curve.

Unsteady large-scale structures have been previously identified by various authors using experimental rigs and computational fluid dynamics (CFD) simulations operating at different turbine conditions and various purge flowrates [14–16]. A study by Rabs et al. [14] showed that two parallel flows at different speeds, billow and roll-up due to the velocity mismatch. This rolling and billowing behavior is caused by Kelvin-Helmholtz instability. Rabs et al. also showed that velocity mismatches present between the highly swirled flow in the main annulus and lower swirled flow in the rim seal cause large-scale structures to form in the turbine rim seal cavity, which are referred to as cells.

The work by Cao et al. [17] is often credited as one of the first studies to identify the existence of large-scale cell structures in the rim cavity. Through the use of high-fidelity CFD models combined with fast-response pressure measurements, Cao et al. quantified the number of cells in the cavity. In another CFD study by Jakobý et al. [18], they also found the presence of low-pressure cells rotating at 80% of the disk speed. Their study indicated that these cells significantly influence ingestion of main annulus hot gas into the rim seal cavity. Beard et al. [19] found the cell quantity was dependent on sealing flowrate, but the cell speed remained constant at 80% of the disk speed for all sealing flowrates studied. While many of these CFD models used sector models, Wang et al. [20] used URANS on a one-stage full wheel and identified the importance of doing so given better agreement with experimental data. Their results also showed that the cell structures in the rim seal caused by shear flow were consistent with areas of low rim sealing effectiveness.

Hualca et al. [21] evaluated the effect of blade and vanes on large-scale unsteady events. Performing experiments with blades

showed that at specific flowrates an increase in swirl ratio ( $\beta$ ) is observed in the rim seal at the same time a decrease in rim sealing effectiveness is observed. Removal of the blades suppressed this increase in swirl and a monotonic increase in rim sealing effectiveness was observed as purge sealing flow increases.

Most rim seal studies have focused on varying the purge sealing flowrate and the rim axial gap, but the inclusion of more complex, engine-realistic cooling, and geometric features is lacking from the literature. As an example, VTE flow is present in most modern gas turbines, which affects the vane–blade flow interactions. In a study conducted within the same facility as that used in the current paper, Monge-Concepción et al. [22] found the presence of VTE flow in the rim seal region using a CO<sub>2</sub> flow tracing method. At low purge flowrates, the presence of VTE flow in the rim cavity increased, due to low rim seal cavity pressure allowing ingestion into the rim seal. URANS modeling also showed the presence of VTE flow in the rim cavity and showed that part of the VTE flow closest radially to the vane hub partially mixes with the main gas path flow prior to ingestion into the rim seal cavity.

Presently, many seal geometries and cooling conditions show good agreement with simplified models, but under certain conditions, a combination of vane–blade interaction and cavity instabilities cause unpredicted behavior in the sealing effectiveness curve. The current study adds to the collection of work on rim events by building an additional understanding of the critical vane–blade interaction through the use of time-resolved measurements in the presence of VTE flow. Unsteady pressure events are correlated to ingress in the cavity by incorporating both high-frequency pressure and high-frequency temperature sensors.

## Experimental Setup

The study presented in this paper was performed at Pennsylvania State University within the Steady Thermal Aero Research Turbine (START) Lab. At the center of the lab is an open-loop, continuous-duration test rig with a single-stage turbine designed to operate at engine-relevant Reynolds and Mach numbers using real hardware. This facility was designed to study and incorporate improvements in under-platform sealing, cooling technologies, additive manufacturing, and novel instrumentation development. The design of the turbine facility is described in detail by Barringer et al. [23].

Figure 1 shows the main components of the START facility. Two industrial compressors powered by separate 1.1 MW (1500 hp) motors supply compressed air to the turbine main gas path (MGP) and secondary air system, for a combined air flowrate up to 11.4 kg/s (25 lbfm/s). Each compressor can discharge flow at 480 kPa and 395 K (70 psig and 250 °F). The compressor discharge

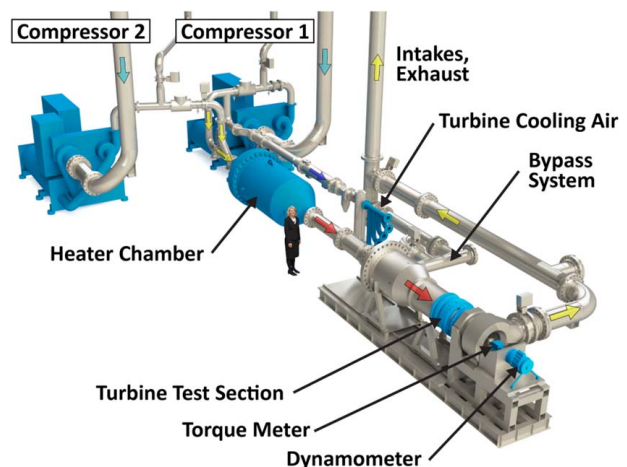


**Fig. 1 START facility overview highlighting the main components in this study**

air to be used in the turbine's main gas path is heated to test conditions using a 3.5-MW inline natural gas heater. The heater is capable of increasing the compressor discharge air temperature from 390 K to 670 K (250–750 °F).

The secondary air system is supplied by a fraction of the compressor discharge flow. This secondary flow is thermally conditioned by a shell-and-tube heat exchanger that cools the air temperature to 273 K (32 °F). This secondary air is subsequently distributed to multiple independently controlled and metered cooling flow streams and then delivered to several locations within the turbine test section.

**Description of Test Turbine.** The test section for the experiment is shown in Fig. 2. The single-stage turbine comprises a true-scale vane and blade representative of a modern aero gas turbine. The work presented in this paper focuses on the rim seal measurement plane denoted in Fig. 2 as “time-resolved sensor location” ( $r/b = 0.98$ ). The rim seal in this study is defined from the pre-swirl discourager ( $r/b = 0.96$ ) to the inner diameter of the vane platform ( $r/b = 0.99$ ). The minimum seal clearance,  $s_c$ , is at the interface of the rim seal and main gas path measuring  $s_c/b = 0.1$ . Further details about the cavity geometry are given by Robak et al. [24].

In this study, purge flow enters the cavity axially through a set of 150 circumferentially spaced holes fed by a vane under the platform plenum. Because the testbed incorporates true-scale engine hardware, the injected coolant flow can go into the cavity, through the blade's internal flow path, or radially inward. Understanding this complex flow with engine parts at engine-realistic conditions makes this data set particularly unique.

The vane ring contains engine-run hardware as well as several “doublets” that were additively manufactured through a metal sintering process. Of the additive doublets, two contain internal passageways for low-frequency pressure and gas concentration measurements, and one is specifically designed for high-frequency measurements of temperature and pressure in the rim seal region. All of the vanes include VTE cooling in the form of radially spaced coolant holes spanning from the hub to the tip of the airfoil fed by a plenum radially outboard of the vane ring. Aside from the VTE cooling passages, the vanes and blades in this study operate as uncooled airfoils.

**Facility Instrumentation.** The test section is highly instrumented, and the measured quantities relevant to this study are highlighted in Fig. 2. The inlet plane's total temperature and total

pressure are measured through a series of 12 sensors (six temperature and six pressure) around the annulus approximately eight axial chords upstream of the vane. The main gas path and coolant flows are measured through Venturi flowmeters upstream of the test section. Additional pressure and temperature sensors located at the inboard coolant plenum characterize the purge flow.

Additionally, this study utilized both high-frequency pressure transducers and high-frequency temperature sensors to quantify time-resolved events. Figure 3(a) shows the locations for the rim seal, rim cavity, and main gas path sensors. Fast-response pressure transducers were installed in locations A (rim seal), E (vane platform), and G (vane tip). A thin film resistive temperature sensor was installed at location A between pressure sensors A2 and A3 as shown in the snippet at the bottom of Fig. 3(b). This temperature sensor was designed and fabricated using nanofabrication infrastructure at Penn State [25].

A total of ten high-frequency response, piezo-resistive pressure transducers were installed in the instrumented vane as shown in Fig. 3(b). These high-frequency response pressure transducers exhibit a usable bandwidth that is several times larger than the blade passing frequency, and more than 20 times greater than the primary frequencies of interest for this study. Six transducers were installed in the circumferential direction at location A (identified as A1 through A6) at a radial distance of  $r/b = 0.98$ . Three transducers were installed at location E (identified as E1 through E3) at a radial distance of  $r/b = 0.99$ . The last transducer was installed at location G. Each of the transducers installed at location A is circumferentially separated by one-fifth of a vane pitch ( $S/5$ ) while transducers at location E are separated by one-half of a vane pitch ( $S/2$ ), where  $S$  represents the vane pitch. Multiple circumferentially distributed sensors installed at each radial location enable the capture of unsteady pressure phenomena propagating tangentially in the cavity. Signals from all fast-response sensors were simultaneously sampled at 100 kHz with analog low-pass filtering to prevent aliasing. A once-per-revolution laser shaft-encoder was installed to enable accurate angular phasing of the sensor signals.

The sensors were fully installed with the vane hardware, and then the instrumented vane assembly was calibrated using a custom pressure vessel with hermetic wire egress. The pressure vessel was then situated in a scientific convection oven with a stability rating of 0.2 K for calibration. Additional ports on the pressure vessel permitted the installation of a pressure controller line (accuracy of 0.14 kPa) as well as a precision resistance temperature detector (RTD) (accuracy of 0.005 K). The temperature and pressure of the system were automatically swept through predetermined

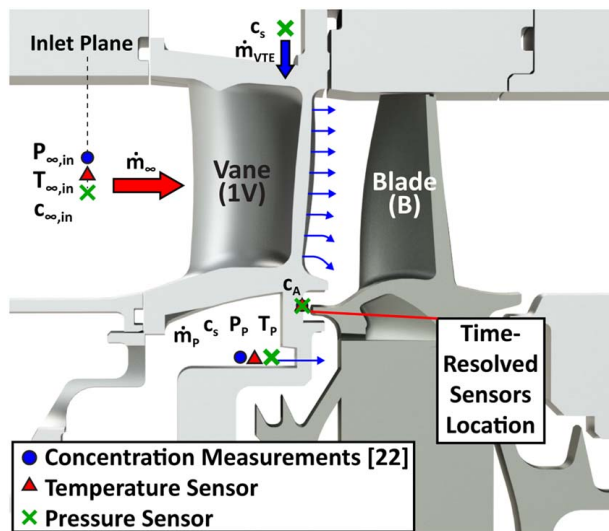


Fig. 2 Diagram of the START test turbine showing the radial distribution of sensors

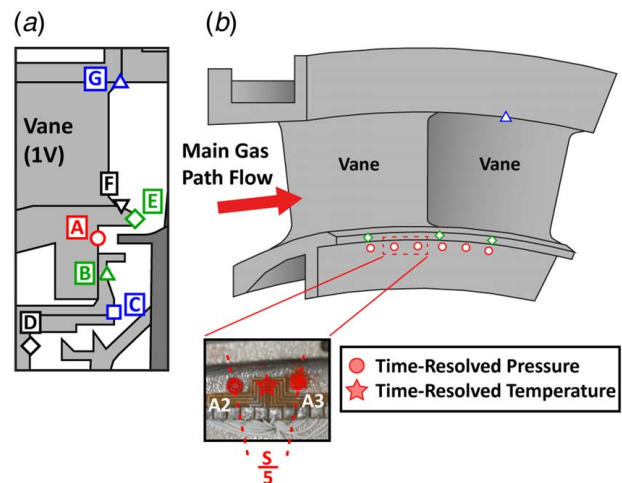


Fig. 3 Diagram of (a) rim seal, rim seal cavity, and main gas path sensor locations and (b) back view of the instrumented vane showing fast-response pressure and temperature sensors in the radial and circumferential locations

setpoints covering the range of thermodynamic states seen through the experiment. To minimize uncertainty in the results, the same sensor leads, excitation channels, and data acquisition channels were matched for calibration and experiment. A calibration surface was fitted that is both a linear fit with pressure and temperature. To determine the pressure from the surface, the voltage was measured, and the temperature was approximated using the nearby high-frequency temperature sensor. Further details of the calibration process are described by Siroka et al. [5].

Rim cooling effectiveness data previously reported by Monge-Concepción et al. [22] showed the importance of vane trailing edge flow. Rim cooling effectiveness,  $\varepsilon_{cc}$ , is defined by Eq. (1)

$$\varepsilon_{cc} = \frac{c_A - c_{\infty, in}}{c_s - c_{\infty, in}} \quad (1)$$

where  $c_A$  is the local concentration of the CO<sub>2</sub> seed gas measured at location A (rim seal) as shown in Fig. 3(a),  $c_s$  is the source concentration of the CO<sub>2</sub> seed gas measured in both the vane underplatform plenum and VTE plenum, and  $c_{\infty, in}$  is the background concentration of CO<sub>2</sub> gas measured at the inlet of the turbine vane in the main gas path.

To determine rim cooling effectiveness, CO<sub>2</sub> was injected into the secondary air (purge and/or VTE flow) to yield a supply CO<sub>2</sub> concentration of 1% within each plenum, respectively. Total pressure probes with Kiel's heads were positioned upstream of the turbine vane inlet and were used to sample airflow in the main gas path to determine background inlet CO<sub>2</sub> concentration ( $c_{\infty, in}$ ). CO<sub>2</sub> concentration was sampled from various circumferentially positioned pressure taps at location A in the vane to determine local concentration ( $c_A$ ). By definition, rim cooling effectiveness ranges from zero to one, where a value of zero represents the full presence of main gas path flow and a value of one represents the full presence of cooling flow in the rim cavity.

**Turbine Operating Point.** The turbine operating point for the present study represents the same test conditions described by Monge-Concepción et al. [22], supporting a back-to-back comparison with previously defined rim cooling effectiveness ( $\varepsilon_{cc}$ ). Flow conditions were held steady throughout the experiment, except for the purge and VTE flowrates, which were varied to determine relative influences on the rim seal flow field. Cooling flowrates presented in this paper are scaled cooling flowrates,  $\Phi/\Phi_{ref}$ , where  $\Phi$  is the cooling flowrate for either purge or VTE flow and  $\Phi_{ref}$  is the reference flowrate defined as the purge flowrate required to fully seal the rim cavity (location C in Fig. 3(a)). Table 1 shows the turbine operating point throughout all the test conditions presented in this study.

To systematically study the effect of purge flow and vane trailing edge flow on rim seal ingestion behavior, two controlled cooling flow configurations were used. Table 2 outlines the two cooling flow configurations named Baseline and Nominal VTE. By comparing the two configurations, it is possible to study the effect of introducing VTE flow over a range of purge flowrates to examine the relative differences in rim seal unsteadiness.

**Measurement Uncertainty.** An uncertainty analysis was performed according to the method outlined by Figliola and Beasley [26] where values shown include bias and precision uncertainty for each parameter. Table 3 shows uncertainties for the turbine

**Table 1 Turbine operating conditions**

Parameters	Symbol	Value
Vane inlet Mach number	—	0.1
Vane inlet axial Reynolds number	$Re_x$	$1.1 \times 10^5$
Blade inlet axial Reynolds number	$Re_x$	$1.1 \times 10^5$
Rotational Reynolds number	$Re_\phi$	$4.0\text{--}9.6 \times 10^6$
Density ratio	$\rho_P/\rho_\infty$	1.0–2.0

**Table 2 Cooling flow configurations**

Configuration name	$\Phi_P/\Phi_{ref}$	$\Phi_{VTE}/\Phi_{ref}$
Baseline	0.4–1.3	0.0
Nominal vane trailing edge	0.4–1.3	0.4

operating parameters and pressure transducer data using the maximum facility capability as the reference condition. To reduce uncertainty of the pressure transducer data, each time-resolved data point presented in this study represents 500 disk revolutions of continuous measurements.

## Computational Model

An unsteady Reynolds-averaged Navier–Stokes (URANS) analysis was performed to compare with experimental results and to further understand the time-resolved flow conditions in the rim seal cavity. The computational model represents the full turbine stage with relevant cavity geometries to accurately capture the main gas path and rim seal cavity flow interactions.

A quarter-wheel circumferential sector of the turbine stage geometry was modeled and meshed using commercial software [27]. The mesh was then exported to a commercial CFD code [28] and its URANS solver was used to fully capture unsteady phenomena in the rim seal cavity. The turbulence model used in this study was the k- $\omega$  shear stress transport (SST) model. Details of the meshing process, mesh quality and independence, turbulence model settings, model validations and equations of state are described in further detail by Robak et al. [24].

The flow conditions simulated in the CFD model are the same as those described in the previous section. The simulations were initially converged using a Reynolds-averaged Navier–Stokes (RANS) solver. Time-resolved simulations were then conducted using the URANS solver for a total of five (5) fully converged disk rotations. Monitor points were positioned at the same locations as the pressure transducer sensors in the experimental test article, as shown in Fig. 3(b). Simulations were considered converged when the pressure amplitudes at the monitor locations were within 5% of the previous revolution value, as further described by Robak et al. [24].

## Impact of Vane Trailing Edge Flow on Steady Cavity Performance

Previous tracer gas measurements by Monge-Concepción et al. [22] qualitatively showed that VTE flow is ingested into the underplatform wheel space, but the study did not directly quantify the thermal benefit or detriment to the cavity performance. Figure 4 displays both the cooling effectiveness,  $\varepsilon_{cc}$  (filled markers), described

**Table 3 Measurement Uncertainties**

Parameter	Symbol	Value
Main gas path flowrate	$\dot{m}/\dot{m}_{ref}$	$\pm 0.004$
Shaft rotational speed	$\Omega/\Omega_{ref}$	$\pm 0.001$
Pressures	$P/P_{ref}$	$\pm 0.001$
Temperatures	$T$	$\pm 0.4$ K
1.0 Stage pressure ratio	$PR/PR_{ref}$	$\pm 0.005$
Purge flowrate	$\dot{m}_P/\dot{m}_{ref}$	$\pm 0.018$
Pressure coefficient	$C_p$	$\pm 0.00005$
Rim cooling effectiveness	$\varepsilon_{cc}$	$\pm 0.015$ to $\pm 0.05$
Time-resolved pressure	$P_{A1-A6}/P_{ref}$	$\pm 0.0035$
Cooling efficiency	$\theta$	$\pm 0.026$ to $\pm 0.061$
Normalized cooling efficiency	$\theta^*$	$\pm 0.0057$
Normalized pressure coefficient	$C_p^*$	$\pm 0.00005$
Nondimensional purge flowrate	$\Phi_P/\Phi_{ref}$	$\pm 0.018$

in the previous section and the thermal efficiency of the cavity  $\theta$  (open symbols) defined in Eq. (2)

$$\theta = \frac{T_{\infty, in} - T}{T_{\infty, in} - T_P} \quad (2)$$

where  $T_{\infty, in}$  is the background temperature at the inlet of the main gas path,  $T$  is the rim seal vane temperature, and  $T_P$  is the purge plenum temperature. These parameters are shown as a function of the nondimensional purge flowrate,  $\Phi_P/\Phi_{ref}$ . The dashed lines in Fig. 4 represent cases without VTE flow and the solid lines represent cases with VTE flow. Accompanying the experimental measurements, Fig. 4 contains the CFD predictions for  $\Phi_P/\Phi_{ref}=0.7$  with and without VTE flow shown as a star and diamond, respectively. Note the agreement between the experiment and computation. These results will be discussed in further detail later.

Several key points are illustrated in Fig. 4. First, the presence of VTE flow increases  $\epsilon_{cc}$  for all flowrates tested, as highlighted by Monge-Concepción et al. [22]. This observation independently confirms ingestion of VTE flow into the under-platform region. The presence of the VTE flow acts to cool the cavity across the range of  $\Phi_P/\Phi_{ref}$ , as shown in Fig. 4 by an increase in  $\theta$  of 7–10%.

The VTE presence allows two mechanisms to work together to impact the cavity temperature. First, when the coolant flow is injected into the vane, the entire airfoil temperature decreases due to conduction. The conduction path through the vane and into the cavity impacts thermal efficiency. Second, the additional airflow in the cavity changes the fluid dynamics, increasing heat transfer by convection. Although the present study cannot distinguish the individual contributions of the VTE flow, the combined effect demonstrates that cooled turbine designs can accommodate ingress that is not necessarily a detriment—an observation that may be counter to traditional cavity design criteria.

The primary goal of cavity design is to prevent ingress of hot gas path air to keep critical inner radius components cool. Concentration measurements quantify the cavity sealing performance but must infer how sealing effectiveness relates to cavity temperature. Therefore, a cavity should be quantified by coupling cooling effectiveness measurements with thermal efficiency measurements. The added benefit of the thermal sensor links ingestion to temperature, more clearly connecting ingestion to component durability as shown in this data set.

Figure 4 contains an inflection in rim cooling effectiveness which spans the purge flowrates of  $0.6 < \Phi_P/\Phi_{ref} < 0.9$ . In this region, increasing the coolant flowrate has a minimal impact on the cooling effectiveness of the cavity. This phenomenon has also been identified in previous studies [20,21], and it has been

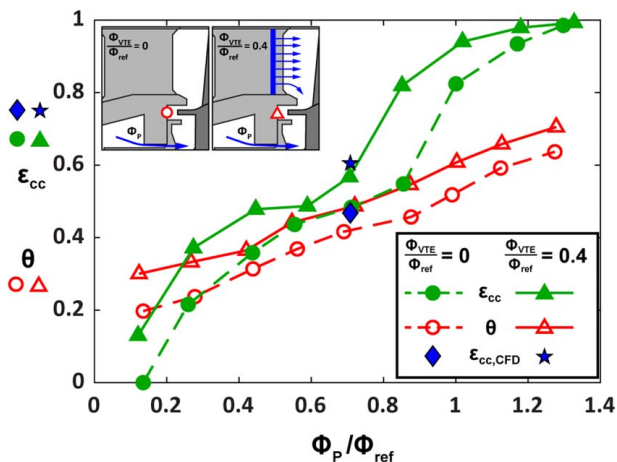


Fig. 4 Thermal efficiency and cooling effectiveness [22] as a function of nondimensional purge flowrates with and without VTE flow

associated with time-varying flow variations in the cavity. Therefore, it is important to understand how the steady cooling effectiveness and thermal efficiency measurements relate to time-varying events.

Furthermore, the addition of VTE flow shifts the onset of this inflection region to higher purge flowrates in Fig. 4. This observation suggests that the VTE flow, which affects the vane-blade interaction, also influences ingestion mechanisms. Current cavity effectiveness models [29,30] do not account for external cooling flows, such as VTE flow, nor do they explain the inflection region. Nonetheless, most modern gas turbines include VTE flow to fill the pressure deficit case by the vane wake in the turbine annulus. Therefore, it is critical to understand both steady and time-resolved interactions of VTE flow with the cavity.

## Correlation of Time-Resolved Measurements and Rim Sealing

Time-resolved pressure and temperature measurements allow a methodology of correlating cavity pressure and temperature to ingress. Following this methodology, which is subsequently outlined, it is shown that fluidic structures with the largest impact on ingestion are present in the inflection region shown in Fig. 4.

Figure 5 presents normalized temperature,  $T'$ , and normalized pressure coefficient,  $C'_p$ , over one rotor revolution for a purge flowrate of  $\Phi_P/\Phi_{ref}=0.7$  in the nominal VTE configuration as shown in Fig. 5. This single test condition was chosen to highlight flow features near the inflection region and serves as an example for the analysis. The data sets were normalized by the minimum and maximum of the data set such that the normalized quantity  $X'$  is represented as

$$X' = \frac{X - X_{min}}{X_{max} - X_{min}} \quad (3)$$

where  $X$  represents the parameter of interest, such as rim seal vane metal temperature and pressure coefficient. It should be noted that the data presented in this section were filtered during post-processing using a zero-phase low-pass digital filter at  $ff_D = 20$  to remove the blade passing events and other high-frequency noise contributions. Through this filtering process, the remaining low-frequency oscillation patterns were identified.

Several significant flow characteristics are shown in the time-resolved pressure and temperature displayed in Fig. 5. First, there is a driving frequency at approximately  $ff_D = 5$  as seen by the five peaks over the rotation in the pressure sensor ( $C'_{p,A2}$  shown in red) as well as the temperature sensor ( $T'$  shown in dashed black lines). Second, the temperature and pressure of these peaks are out of phase. The temperature phase lag,  $\Psi_T$ , is defined as the

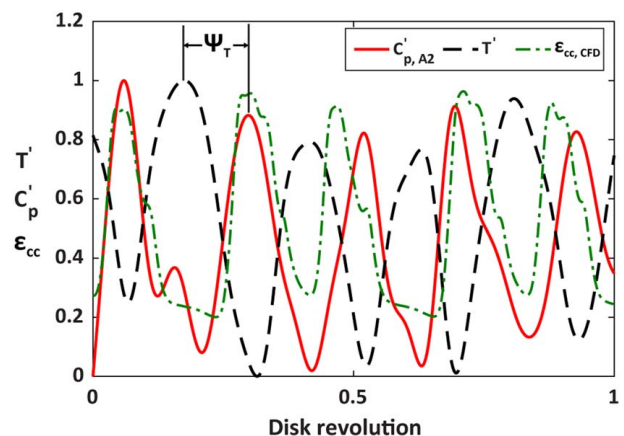


Fig. 5 Time trace of normalized parameters measured at  $\Phi_P/\Phi_{ref}=0.7$  and  $\Phi_{VTE}/\Phi_{ref}=0.4$

shift of the temperature trace to the pressure trace in degrees and is explicitly called in Fig. 5.  $\Psi_T$  is an important parameter because it correlates pressure to temperature. Specifically, when the pressure and temperature are out of phase, it indicates time-varying ingress in the cavity. One purpose of the coolant is to pressurize the cavity, sealing it from main gas path ingestion. This means a local maximum of pressure indicative of coolant should coincide with a local minimum in temperature, as shown in Fig. 5.

Figure 5 also shows the rim cooling effectiveness ( $\epsilon_{cc}$  shown in dashed green lines) at location A using the URANS simulation. Results in Fig. 5 indicate that a rise in the local coefficient of pressure corresponds to a rise in the rim cooling effectiveness, and similarly a decrease in local pressure yields a decrease in rim cooling effectiveness. Given the matched periodicity between the effectiveness and pressure curves, the CFD results point to the cells as being a clear contributor to the ingestion process into the rim seal region.

To improve understanding of the unsteady flow effects that contribute to ingestion, the time-resolved pressure data measured from the high-frequency response sensors were analyzed using discrete Fourier transforms. Previous authors [13,15,16,18] have identified large-scale cell structures rotating in the rim seal at frequencies well below the blade passing frequency (BPF). Results shown so far indicate that the inflection region in rim cooling effectiveness ( $0.6 < \Phi_p/\Phi_{ref} < 0.9$ ) is of particular interest since it diverges from established hot gas ingestion models. Therefore, the time-resolved measurements within this region are analyzed in the following figures.

Discrete Fourier transforms (DFT) for the purge flowrates corresponding to the cooling effectiveness inflection region are shown in Figs. 6(a)–6(f). These DFTs were computed using an iterative zero-padding routine to ensure peak value convergence [5]. However, after all cases were computed, the data were normalized by the absolute maximum amplitude across all test cases. Unlike  $X'$ , which is normalized across a single flow condition,  $X^*$  is normalized across all test conditions for relative comparison. For each graph, the dashed lines represent cases without VTE flow, and the solid lines represent cases with VTE flow.

The inflection region data presented in Figs. 6(a)–6(f) exhibited the largest amplitude peaks over all evaluated test conditions. Figures 6(a)–6(f) show that large amplitude values in  $C_p^*$

correspond to large amplitudes in  $\theta^*$ , verifying that these pressure variations are moving pockets of cold and warm air. The experimental data appear as discrete spikes of activity near a normalized frequency of  $f/f_D = 5$ . This finding is similar to that of Hualca et al. who attributed the various peaks to be a fluid instability switching between integer pressure cells [21]. However, in contrast to Hualca et al., no clear relationship between the low-frequency spectral peak locations and particular airfoil counts or hardware were identified. The effect of VTE on the time-varying events is also evident comparing the peak amplitudes in Figs. 6(a)–6(f). Specifically, the VTE flow acts to suppress the time-varying instabilities.

The previous section displayed the entire frequency spectra for selected purge flowrates distributed across the inflection region. This section utilizes the maximum amplitude of the frequency spectra to connect the time-varying events to cavity performance as illustrated in Fig. 7. The y-axis in Fig. 7 displays the maximum amplitude normalized cavity efficiency (green dashed lines with stars) and maximum amplitude normalized pressure coefficient (in black and red dashed lines with circles and plus signs respectively) as a function of  $\Phi_p/\Phi_{ref}$ . Additionally, the cooling effectiveness from Fig. 4 is provided as an overlay on the graphs for comparison. Figure 7(a) represents a purge-only configuration without VTE flow, whereas Fig. 7(b) includes the addition of VTE flow. Furthermore, Fig. 7 includes data from three high-frequency sensors (two pressure sensors and one temperature sensor). The independent pressure sensors, which span one-fifth of a vane pitch, qualitatively display the same trend and normalized amplitudes, illustrating the repeatability and relative insensitivity to circumferential location.

At low  $\Phi_p/\Phi_{ref}$  values in Fig. 7, the maximum amplitude of unsteady features is relatively small. However, when approaching the inflection region ( $0.6 < \Phi_p/\Phi_{ref} < 0.9$ ), the largest amplitude features are present and have been shown to indicate ingestion. This time-varying ingestion causes the reduction of sealing performance indicative of the inflection point. As  $\Phi_p/\Phi_{ref}$  increases past the inflection point, the time-resolved amplitudes decrease, and the sealing effectiveness returns to a purely increasing behavior.

In both Figs. 7(a) and 7(b), the normalized amplitudes reach a peak value coincident with the inflection point, as defined by the  $\Phi_p/\Phi_{ref}$  value corresponding to the lowest slope value between neighboring points. Because the inflection point occurs at different

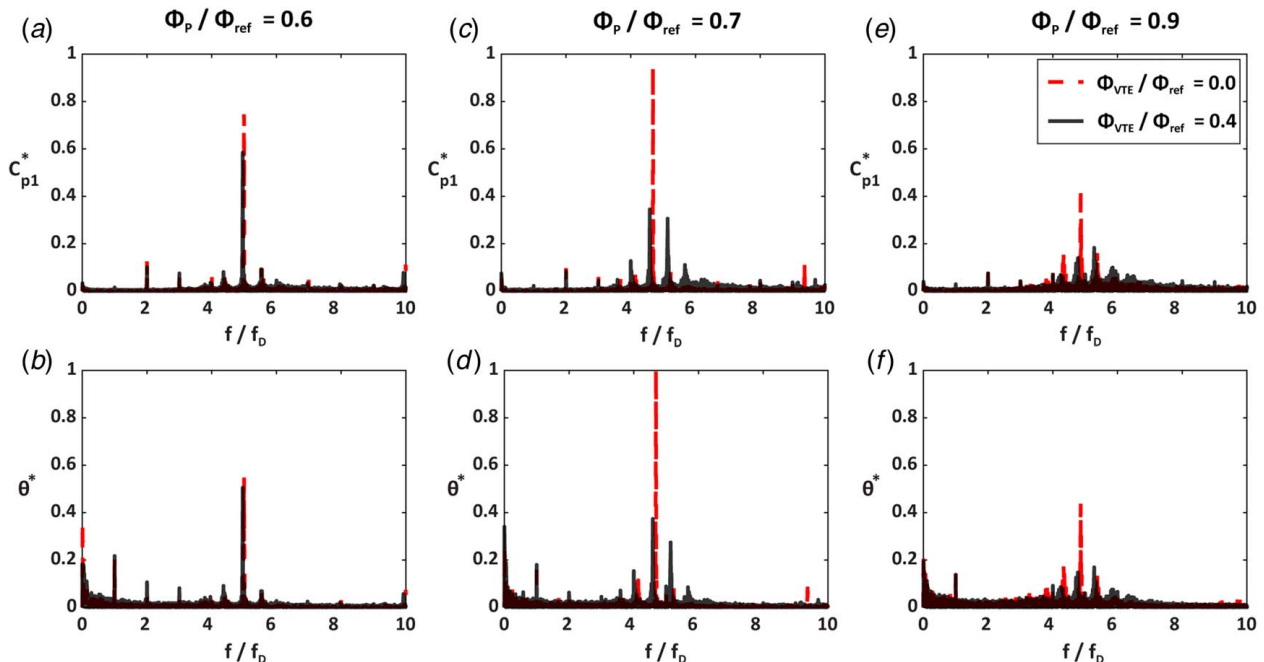
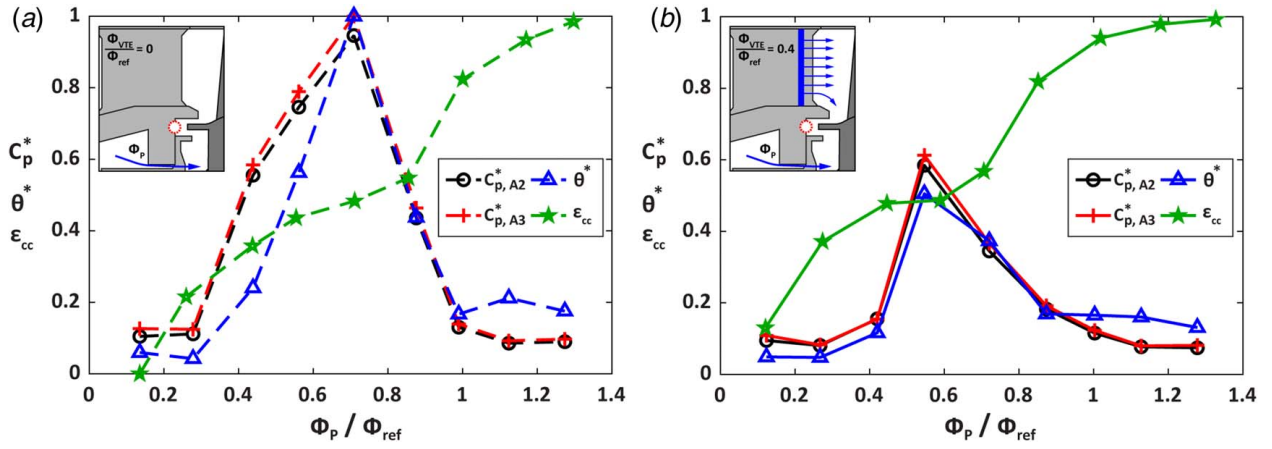


Fig. 6 Discrete Fourier transforms of normalized pressure coefficient and thermal efficiency for inflection region purge flowrates of  $\Phi_p/\Phi_{ref} = 0.6$  (left column),  $\Phi_p/\Phi_{ref} = 0.7$  (center column), and  $\Phi_p/\Phi_{ref} = 0.9$  (right column)



**Fig. 7** Maximum amplitude of normalized pressure coefficient ( $C_p^*$ ), cavity temperature efficiency ( $\theta^*$ ), and cooling effectiveness ( $\epsilon_{cc}$ ) for the (a) baseline and (b) nominal VTE configurations

nondimensional purge flowrates for the two cases, this finding directly connects the inflection location to maximum unsteady amplitude, not a particular  $\Phi_p/\Phi_{ref}$  value.

Comparing Figs. 7(a) and 7(b), the presence of VTE flow also reduces the amplitude of the time-resolved pressure and temperature. Quantitatively, the maximum peak between the two cases is reduced by 50% in the temperature and 40% in the pressure. Although not explicitly shown here, accompanying simulations provide insight into this behavior. Near the main gas path endwalls, VTE flow propagates downstream allowing the VTE flow to enter the cavity in relatively high concentrations. This additional flow changes the cavity dynamics and hence the instability onset and strength [5]. Interestingly, the inflection of the curve is equally pronounced for both cases, with and without VTE flow, despite the reduction in the unsteady amplitudes. Although this approach of linking a single frequency and amplitude to the sealing effectiveness may be an oversimplification of the complex flow physics present in the rim seal region, it provides a method to connect time-varying events with steady sealing performance. Connections such as these are important to developing real-time turbine health monitoring [31].

### Characterization of Under-platform Flow Structures

Spectral transforms of the pressure sensor data support the identification of the different frequencies and amplitudes of the flow cells that promote detrimental main gas flow ingestion into the rim seal. Additional flow characteristics were also determined by using the pressure signals from at least two pressure transducers at each radial location to quantify the cell structure tangential speed and count. Examples of both the raw and the filtered signals from the fast-response pressure transducers in the rim seal are shown in Fig. 8. The raw pressure signals shown correspond to sensors A1, A2, A3, and A6 over one full disk revolution for the Baseline flow configuration with  $\Phi_p/\Phi_{ref}=0.4$  and  $\Phi_{VTE}/\Phi_{ref}=0.0$ . To provide additional context, pressure signals in Fig. 8 were normalized to a dynamic pressure based on the purge flow conditions and disk speed ( $0.5\rho_p\Omega^2b^2$ ).

The raw data signals shown in Fig. 8 include high-frequency fluctuations caused by blade passing events, which are superimposed onto the low-frequency waveforms associated with the rotating large-scale cells. A digital Butterworth low-pass filter (green line) was used with a cutoff frequency of  $15f_D$ , to more easily visualize the low-frequency oscillations, similar to the approach used by Cameron [32] and Berdanier et al. [33]. The cutoff frequency of  $15f_D$  was selected as a point above the primary frequency contributors, including unsteady ingestion patterns, but below the primary blade passing frequency.

Through comparison of the filtered signals in Fig. 8, the pressure peak for each subsequent sensor at location A is slightly offset in time (normalized rotation position) from previous sensors as shown by the red arrows in Fig. 8. As these unsteady cells in the rim seal rotate tangentially in the direction of the disk rotation, they create alternating pressure fluctuations that are registered by the pressure transducers. Using two circumferentially spaced transducers, it is possible to calculate the time ( $\Delta t$ ) it takes for a fluid cell to pass from one transducer to the next transducer. A cross-correlation, the measure of similarity between data signals from two sensors, was used to determine the time delay,  $\Delta t$  between two sensor locations.

To calculate these properties, three parameters must be known including the angle between transducers ( $\alpha$ ), the peak frequency ( $f_{peak}$ ), and the delay time ( $\Delta t$ ) between the peak frequency on one transducer to the next transducer. Peak frequency is defined as the frequency corresponding to the maximum pressure amplitude during one full disk revolution.

A phase analysis to determine the cell speed ( $\Omega_S$ ) and count ( $N_S$ ) was performed using the methodology described by Beard et al. [19]. Equations (4) and (5) were used to determine the cell tangential speed and count, respectively

$$\Omega_S = \frac{\alpha}{\Delta t} \quad (4)$$

$$N_S = \frac{2\pi f_{peak}}{\Omega_S} \quad (5)$$

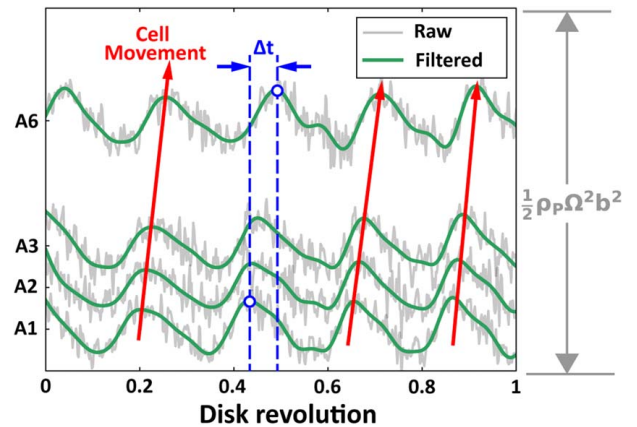


**Fig. 8** Fast-response pressure data plotted versus normalized rotational position showing raw and filtered signals in the rim seal at a purge flowrate  $\Phi_p/\Phi_{ref} = 0.4$

Results presented for both cell speed and count are based on data samples that span 500 disk revolutions. Figure 9 shows the large-scale cell speed ( $\Omega_s$ ) for the rim seal and vane platform for both the Baseline and the Nominal VTE flow configurations at locations A and E. The cell speed is nondimensionalized by the disk rotational speed ( $\Omega_D$ ). The cell speed shown in Fig. 9 is calculated using transducer pairs A1–A6 and E1–E3, which are both separated by exactly one vane pitch. By using these transducer pairs, the pitch-average cell speed and count were determined at the purge flowrate and VTE flowrates shown in Table 2.

Inspection of the results in Fig. 9 shows that an increase in purge flow, regardless of locations A or E and VTE flowrate, decreases the cell speed at both radial locations. The cell speed ranges from approximately 80% of the disk speed, at the lowest purge flow, down to nearly 45% of the disk speed at the highest purge flowrate. These relative cell speeds are consistent with previous experimental and computational studies [17,19,21,34] that report cells rotating at a fraction of the disk speed. In these studies, it was shown cells rotate at speeds of  $\sim 80\%$  to  $\sim 95\%$  of the disk speed. Figure 9 shows that the presence of VTE flow has a marginal effect on the cell tangential speed. This means that the flow field interaction between the MGP rim seal is mostly unchanged such that the VTE flow mostly mixes with the annulus flow.

Figure 10 shows the radial distribution ( $r/b$ ) of the average swirl ratio,  $\beta$ , at the tested purge flowrates using CFD. The CFD results presented were taken at the mid-axial plane 50% between the stator wall and the rotor wall as depicted in the inset diagram. For all purge flowrates, the average swirl ratio in the vane platform (location E) is higher than the average swirl ratio in the rim seal (location A). This is caused by the influence of the highly swirled flow in the main gas path annulus, which is closest to location E. As the flow is ingested into the rim seal near location A, the flow loses tangential velocity. Additional CFD analysis at axial positions closer to the stationary vane wall will be performed to determine if the predictions more closely match the cell speed experimental data taken from sensors embedded in the vane wall. Figure 10 shows that swirl velocity in the rim seal and rim cavity decreases for all radial locations since the purge flow is injected through holes that aligned in the axial direction.

Mathematically, normalized cell speed ( $\Omega_s/\Omega_D$ ) and swirl ratio ( $\beta$ ) represent similar characteristics. If the cells are moving at a

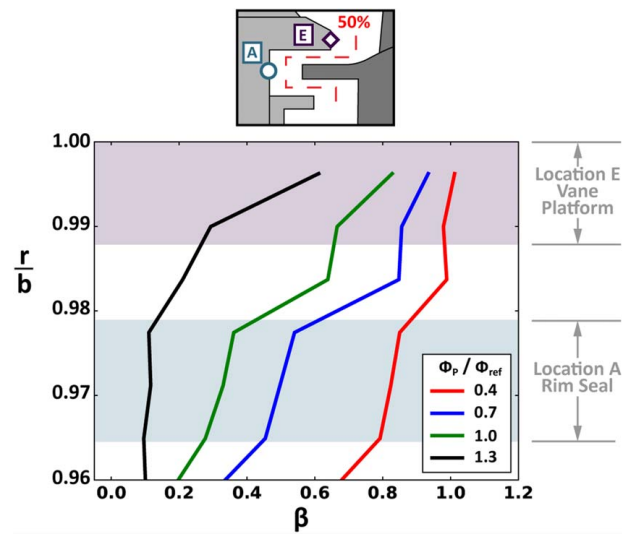


Fig. 10 Radial distribution of swirl ratio ( $\beta$ ) at various purge flowrates ( $\Phi_p/\Phi_{ref}$ ) using URANS CFD simulations

tangential velocity which is equal to the bulk tangential velocity in the rim seal, then the cell speed,  $\Omega_s$ , is representative of the tangential bulk fluid velocity,  $V_\phi$ . In this case, the cell speed measured by a fast-response pressure sensor can be an indicator of swirl ratio, a critical parameter for rim sealing performance. Additional follow-on work beyond the initial scope of this study is required to validate such approximations, including an assessment of cell position in the rim seal.

Pitch-average cell count ( $N_s$ ) is plotted in Fig. 11 at the tested purge flowrates and VTE flowrates in Table 2. It can be observed that as the purge flowrate increases, there is an increase in the number of cells present in the platform (location E) and front rim seal region (location A). This result confirms the theoretical trend from Eq. (5) that cell speed ( $\Omega_s$ ) has an inverse relation to the number of cells ( $N_s$ ). The pitch-average cell count increases from approximately 6 cells at the lowest purge flowrate (for both locations A and E), to near 17 cells when the rim seal is fully sealed.

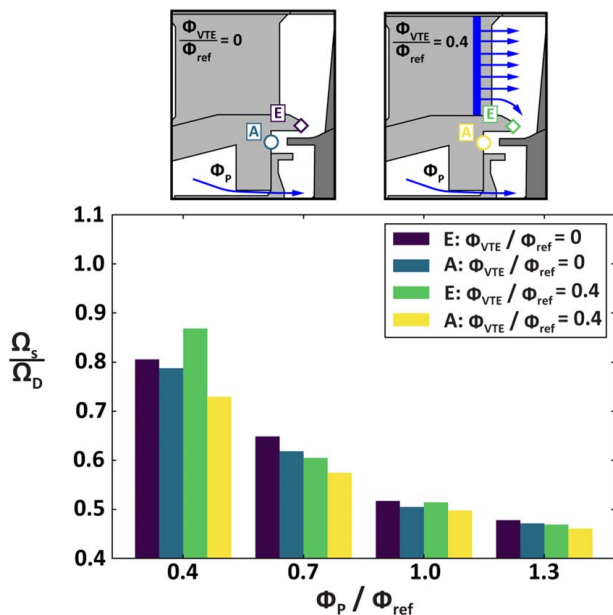


Fig. 9 Pitch-average normalized cell speed ( $\Omega_s/\Omega_D$ ) for the baseline and nominal VTE configurations at locations A and E from the experiment

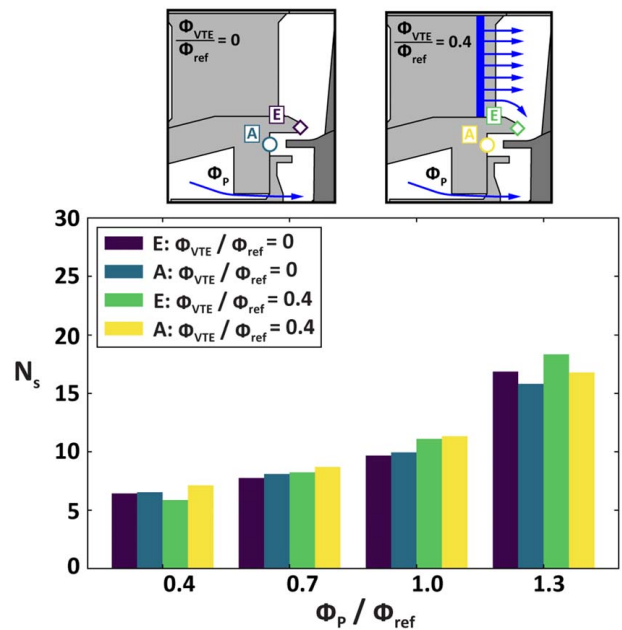
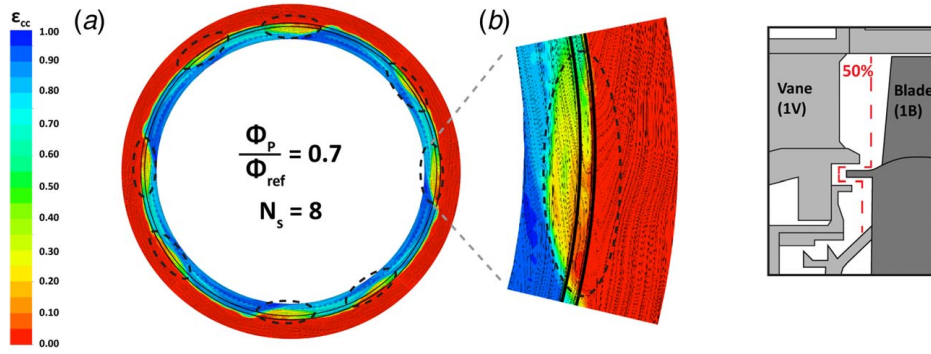
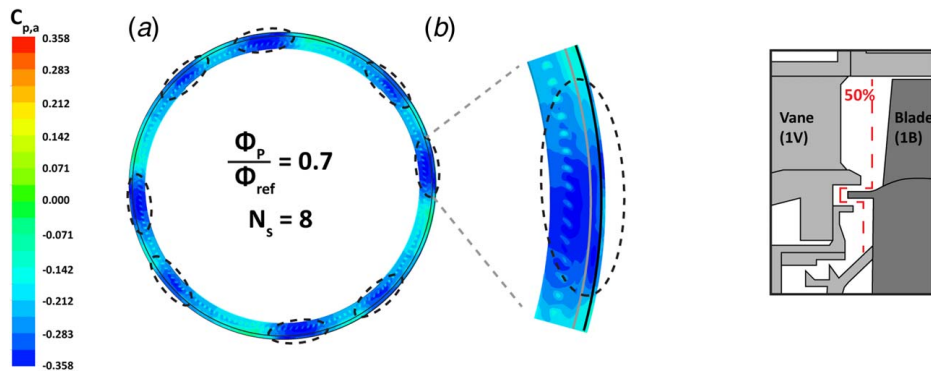


Fig. 11 Pitch-average cell count ( $N_s$ ) for the baseline and nominal VTE configurations at locations A and E from the experiment



**Fig. 12** Rim cooling effectiveness ( $\epsilon_{cc}$ ) at a purge flowrate of  $\Phi_p/\Phi_{ref} = 0.7$  and VTE flowrate  $\Phi_{VTE}/\Phi_{ref} = 0$  depicting (a) full-wheel results and (b) a magnified section of the wheel showing the recirculation zone



**Fig. 13** Coefficient of pressure ( $C_{p,a}$ ) at a purge flowrate of  $\Phi_p/\Phi_{ref} = 0.7$  and VTE flowrate  $\Phi_{VTE}/\Phi_{ref} = 0$  depicting (a) full-wheel results and (b) a magnified section of the wheel showing the recirculation zone

It must be noted that when calculating the number of cells present at a specific purge flowrate, the number of cells calculated is not necessarily an integer number. It is hypothesized that the presence of a partial cell is a consequence of individual cells forming and deforming (vortex shedding) in the rim seal as they continuously rotate.

An increase in the cell number occurs due to the purge flow changing the flow field in the rim seal from a highly swirled flow to lower swirl velocity as was shown in Fig. 10. This causes a rise in the difference between the swirl velocity in the main gas path annulus and the rim seal, which suggests increased shear flow between the main annulus flow and the rim seal flow. Increased shear flow influences the formation of instabilities.

The number of large-scale structures present in the rim seal can be clearly observed from the URANS simulations presented in Figs. 12 and 13. The CFD results in Figs. 12 and 13 were generated from quarter-wheel simulations with periodic boundary conditions. Further details about the CFD method are given by Robak et. al [24]. Figure 12 shows rim cooling effectiveness ( $\epsilon_{cc}$ ) along with streamlines in the main gas path annulus and rim seal from the rotational frame of reference, while Fig. 13 shows the nondimensional coefficient of pressure ( $C_{p,a}$ ). Results in both figures correspond to a purge flowrate of  $\Phi_p/\Phi_{ref} = 0.7$  and a VTE flowrate of  $\Phi_{VTE}/\Phi_{ref} = 0$ . A closeup view illustrating a large-scale structure in the rim seal was also included in Figs. 12(b) and 13(b).

Flow from the highly swirled main annulus encounters lower swirled flow in the rim seal where the velocity mismatch causes the flows to recirculate, in turn forming large-scale structures at the entrance of the rim seal. Inspection of Fig. 12(b) shows that these structures span radially from the vane platform and past the rim seal into the rim cavity. Streamlines show an area of recirculation between the main gas path annulus flow and the rim seal flow.

This recirculation zone lowers local rim cooling effectiveness while deeper in the rim cavity shows a high presence of purge flow.

Large-scale structures can be observed in Fig. 13 at locations where the annulus flow coefficient of pressure  $C_{p,a}$  is less than 0. This relatively low annulus pressure is a driver of local ingestion into the rim seal, which corresponds to the decrease of local rim cooling effectiveness shown previously in Fig. 12(b).

The CFD results presented in this paper provided meaningful insight to further expand understanding of the experimental data. Although 500 disk revolutions were used to determine the minimum-to-maximum ranges in  $\Omega_s$  and  $N_s$  for each test condition, only five revolutions of CFD predictions were analyzed due to the high computational cost. It should be noted that although the CFD simulations were validated with experimental data sets [24], some differences between the CFD and experimental results are present due to the complexity of the geometry and flow fields being modeled. Overall, using CFD simulations aided in accurately capturing the fundamental trends identified by the experimental data.

## Conclusions

This study utilized a single-stage turbine operating with true-scale engine hardware at relevant operating conditions to quantify the effect of coolant flows on the performance of the rim seal region. The steady and time-resolved sealing behavior was quantified using high-frequency pressure and temperature sensors. These data were then compared with CO<sub>2</sub> tracer gas cooling effectiveness measurements for identical conditions.

The comparison of time-resolved measurements with traditional tracer gas sealing quantification shows that VTE flow is ingested

into the cavity and measured an increase in the cavity thermal efficiency to be 7–10% with expected contributions from conduction and convection effects. This finding confirms that VTE provides a thermal benefit to the cavity and should be accounted for in cavity effectiveness modeling to prevent excessive use of purge flow.

The correlation of the pressure coefficient and normalized temperature signals indicates ingress occurs when the two signals are out of phase. This method allows the separation of time-varying events responsible for ingestion from those less detrimental to cavity performance. This dataset showed that nondimensional purge flowrates near the cooling effectiveness inflection region create a fluid instability responsible for time-varying ingestion. A Fourier transform analysis of normalized thermal efficiency and pressure coefficient measurements in this inflection region indicate the presence of low-frequency pressure and temperature peaks corresponding to rotating cells in the cavity. The amplitude of these peaks was suppressed by as much as 50% when VTE was present.

Unsteady large-scale cells in the rim seal were characterized by their tangential speed and quantity. Results show that purge flow is a significant driver in changing the tangential speed and count of these cells. Increasing the purge flowrate decreases the tangential speed of the cells since the purge flow imparts a significant axial momentum to the bulk rim seal flow, whereas increasing the purge flowrate increases the number of cells present in the rim seal, which is thought to be related to an increase in the number of flow instabilities associated with cell formation and deformation. Although VTE flow was shown to suppress the time-varying pressure and temperature signals, this change in amplitude did not significantly affect the count or speed of the rotating cell structures.

Results in this study build upon previous findings in the literature on rim cavity instabilities and how they contribute to ingestion. The current study shows the importance of further understanding the nature and impact of the large-scale, low-pressure structures that were found to drive unsteady ingestion into the rim seal region. Critical insights into the unsteady flow mechanisms influencing ingestion can aid engine designers to improve rim seal geometries that suppress the formation of large-scale cell structures. This work encourages further time-resolved research in the rim seal to develop better design tools to mitigate the effects of hot gas ingestion.

## Acknowledgment

The authors would like to thank Pratt & Whitney and the U.S. Department of Energy National Energy Technology Laboratory for sponsoring the research presented in this paper. This paper is based upon work supported by the Department of Energy under Award Number DE-FE0025011.

## Conflict of Interest

There are no conflicts of interest.

## Data Availability Statement

The authors attest that all data for this study are included in the paper.

## Disclaimer

This report was prepared as an account of work sponsored by an agency of the United States Government. Neither the United States Government nor any agency thereof, nor any of their employees, makes any warranty, express or implied, or assumes any legal liability or responsibility for the accuracy, completeness, or usefulness of any information, apparatus, product, or process disclosed, or represents that its use would not infringe privately owned rights. Reference herein to any specific commercial product, process, or service

by trade name, trademark, manufacturer, or otherwise does not necessarily constitute or imply its endorsement, recommendation, or favoring by the United States Government or any agency thereof. The views and opinions of authors expressed herein do not necessarily state or reflect those of the United States Government or any agency thereof.

## Nomenclature

$b$	= hub radius
$c$	= gas concentration
$f$	= frequency
$r$	= radius
$C$	= chord length
$D$	= disk
$P$	= pressure
$T$	= temperature
$V$	= main gas path velocity
$\dot{m}$	= mass flowrate
$C_p$	= coefficient of pressure, $(P - \bar{P})/(0.5\rho\Omega^2 b^2)$
$s_C$	= seal clearance
PR	= stage pressure ratio
$Re_x$	= axial Reynolds number, $VC_x/\nu$
$Re_\phi$	= rotational Reynolds number, $\Omega b^2/\nu$
$\beta$	= swirl ratio, $V_\phi/\Omega r$
$\epsilon_{cc}$	= cooling effectiveness, $(c - c_{\infty, in})/(c_s - c_{\infty, in})$
$\theta$	= cavity cooling efficiency, $(T_{MGP} - T)/(T_{MGP} - T_P)$
$\rho$	= density
$\nu$	= kinematic viscosity
$\Phi$	= cooling flowrate, $\dot{m}/(2\pi s_C \rho \Omega b^2)$
$\Phi_0$	= Largest flow parameter with zero effectiveness
$\Phi_{min}$	= Minimum flow parameter to seal a given location
$\Phi_{ref}$	= Reference flow rate, $\Phi_{min}$ for Location B at Baseline
$\Omega$	= Angular velocity

## Subscripts, Accents, and Abbreviations

$a$	= annulus
$in$	= inlet conditions
$P$	= purge
$ref$	= generic reference condition
$s$	= supply level
$t$	= total condition
$x$	= axial direction
$\phi$	= tangential direction
$\infty$	= background level
$\cdot$	= average value
$\bar{\cdot}$	= area averaged value
$*$	= normalized over all test conditions
$'$	= normalized over a single test condition

## References

- [1] Air Transport Action Group, 2018, Aviation Benefits Beyond Borders, [https://aviationbenefits.org/media/166344/abb18\\_full-report\\_web.pdf](https://aviationbenefits.org/media/166344/abb18_full-report_web.pdf)
- [2] Bunker, R. S., 2017, "Evolution of Turbine Cooling," Proceedings of the ASME Turbo Expo, Paper No. GT2017-63205.
- [3] Berdanier, R. A., Thole, K. A., Knisely, B. F., Barringer, M. D., Grover, E. A., and Monge-Concepción, I., 2019, "Scaling Sealing Effectiveness in a Stator-Rotor Cavity for Differing Blade Spans," *ASME J. Turbomach.*, **141**(5), p. 051007.
- [4] Clark, K. P., Johnson, D., Thole, K. A., Robak, C., Barringer, M. D., and Grover, E., 2018, "Effects of Purge Flow Configuration on Sealing Effectiveness in a Rotor-Stator Cavity," *ASME J. Eng. Gas Turbines Power*, **140**(11), p. 112502.
- [5] Siroka, S., Monge-Concepción, I., Berdanier, R. A., Barringer, M. D., and Thole, K. A., 2021, "Correlating Cavity Sealing Effectiveness to Time-Resolved Rim Seal Events in the Presence of Vane Trailing Edge Flow," Proceedings of the ASME Turbo Expo 2021, Paper No. GT2021-59285.
- [6] Monge-Concepción, I., Siroka, S., Berdanier, R. A., Barringer, M. D., Thole, K. A., and Robak, C., 2021, "Unsteady Turbine Rim Sealing and Vane Trailing Edge Flow Effects," Proceedings of the ASME Turbo Expo 2021, Paper No. GT2021-59273.

- [7] Johnson, B. V., Mack, G. J., Paolillo, R. E., and Daniels, W. A., 1994, "Turbine Rim Seal Gas Path Flow Ingestion Mechanisms," Proceedings of the 30th AIAA/ASME/SAE/ASEE Joint Propulsion Conference, Paper No. AIAA 94-2703.
- [8] Scobie, J. A., Sangan, C. M., Michael Owen, J., and Lock, G. D., 2016, "Review of Ingress in Gas Turbines," *ASME J. Eng. Gas Turbines Power*, **138**(12), p. 120801.
- [9] Gentilhomme, O., Hills, N. J., Turner, A. B., and Chew, J. W., 2003, "Measurement and Analysis of Ingestion Through a Turbine Rim Seal," *ASME J. Turbomach.*, **125**(3), pp. 505–512.
- [10] Scobie, J. A., Sangan, C. M., Owen, J. M., Wilson, M., and Lock, G. D., 2014, "Experimental Measurements of Hot Gas Ingestion Through Turbine Rim Seals at Off-Design Conditions," *Proc. Inst. Mech. Eng. Part A J. Power Energy*, **228**(5), pp. 491–507.
- [11] Patinios, M., Scobie, J. A., Sangan, C. M., and Lock, G. D., 2017, "Performance of Rim-Seals in Upstream and Downstream Cavities Over a Range of Flow Coefficients," *Int. J. Turbomach. Propuls. Power*, **2**(4), p. 21.
- [12] Patinios, M., Ong, I. L., Scobie, J. A., Lock, G. D., and Sangan, C. M., 2018, "Influence of Leakage Flows on Hot Gas Ingress," Proceedings of the Turbo Expo 2018, Paper No. GT2018-75071.
- [13] Horwood, J. T. M., Hualca, F. P. T., Wilson, M., Scobie, J. A., Sangan, C. M., and Lock, G. D., 2018, "Unsteady Computation of Ingress Through Turbine Rim Seals," Proceedings of the ASME Turbo Expo 2018, Paper No. GT2018-75321.
- [14] Rabs, M., Benra, F. K., Dohmen, H. J., and Schneider, O., 2009, "Investigation of Flow Instabilities Near the Rim Cavity of a 1.5 Stage Gas Turbine," Proceedings of the Turbo Expo 2009, Paper No. GT2009-59965.
- [15] Chilla, M., Hodson, H., and Newman, D., 2013, "Unsteady Interaction Between Annulus and Turbine Rim Seal Flows," *ASME J. Turbomach.*, **135**(5), p. 051024.
- [16] Savov, S. S., Atkins, N. R., and Uchida, S., 2017, "A Comparison of Single and Double Lip Rim Seal Geometry," *ASME J. Eng. Gas Turbines Power*, **139**(11), p. 112601.
- [17] Cao, C., Chew, J. W., Millington, P. R., and Hogg, S. I., 2004, "Interaction of Rim Seal and Annulus Flows in an Axial Flow Turbine," *ASME J. Eng. Gas Turbines Power*, **126**(4), pp. 786–793.
- [18] Jakoby, R., Zierer, T., Lindblad, K., Larsson, J., Devito, L., Bohn, D. E., Funcke, J., and Decker, A., 2004, "Numerical Simulation of the Unsteady Flow Field in an Axial Gas Turbine Rim Seal Configuration," Proceedings of the Turbo Expo 2004, Paper No. GT2004-53829.
- [19] Beard, P. F., Gao, F., Chana, K. S., and Chew, J. W., 2017, "Unsteady Flow Phenomena in Turbine Rim Seals," *ASME J. Eng. Gas Turbines Power*, **139**(3), p. 032501.
- [20] Wang, C.-Z., Mathiyalagan, S. P., Johnson, B. V., Glahn, J. A., and Cloud, D. F., 2014, "Rim Seal Ingestion in a Turbine Stage From 360 Degree Time-Dependent Numerical Simulations," *ASME J. Turbomach.*, **136**(3), p. 031007.
- [21] Hualca, F. P. T., Horwood, J. T. M., Sangan, C. M., Lock, G. D., and Scobie, J. A., 2020, "The Effect of Vanes and Blades on Ingress in Gas Turbines," *ASME J. Eng. Gas Turbines Power*, **142**(2), p. 021020.
- [22] Monge-Concepción, I., Berdanier, R. A., Barringer, M. D., Thole, K. A., and Robak, C., 2020, "Evaluating the Effect of Vane Trailing Edge Flow on Turbine Rim Sealing," *ASME J. Turbomach.*, **142**(8), p. 081001.
- [23] Barringer, M. D., Coward, A., Clark, K. P., Thole, K. A., Schmitz, J., Wagner, J., Alvin, M. A., Burke, P., and Dennis, R., "The Design of a Steady Aero Thermal Research Turbine (START) for Studying Secondary Flow Leakages and Airfoil Heat Transfer," Proceedings of the ASME Turbo Expo 2014, Paper No. GT2014-25570.
- [24] Robak, C., Faghri, A., and Thole, K. A., 2019, "Analysis of Gas Turbine Rim Cavity Ingestion With Axial Purge Flow Injection," Proceedings of the Turbo Expo 2019, Paper No. GT2019-91807.
- [25] Siroka, S., Berdanier, R. A., Thole, K. A., Chana, K., Haldeman, C. W., and Anthony, R. J., 2020, "Comparison of Thin Film Heat Flux Gauge Technologies Emphasizing Continuous-Duration Operation," *ASME J. Turbomach.*, **142**(9), p. 091001.
- [26] Figliola, R. S., and Beasley, D. E., 2014, *Theory and Design for Mechanical Measurements*, John Wiley & Sons, Inc, New York.
- [27] Siemens PLM Software, 2017, "STAR-CCM+ 11.06," Plano, TX.
- [28] ANSYS, 2017, "ANSYS Fluent 18.2," Canonsburg, PA.
- [29] Sangan, C. M., Pountney, O. J., Zhou, K., Wilson, M., Owen, J. M., and Lock, G. D., 2013, "Experimental Measurements of Ingestion Through Turbine Rim Seals-Part I: Externally Induced Ingress," *ASME J. Turbomach.*, **135**(2), p. 021012.
- [30] Sangan, C. M., Pountney, O. J., Zhou, K., Owen, J. M., Wilson, M., and Lock, G. D., 2013, "Experimental Measurements of Ingestion Through Turbine Rim Seals-Part II: Rotationally Induced Ingress," *ASME J. Turbomach.*, **135**(2), p. 021013.
- [31] DeShong, E. T., Peters, B., Berdanier, R. A., Thole, K. A., Paynabar, K., and Gebrael, N., 2021, "Correlating Time-Resolved Pressure Measurements with Rim Sealing Effectiveness for Real-Time Turbine Health Monitoring," ASME Turbo Expo 2021, Paper No. GT2021-59586.
- [32] Cameron, J. D., 2007, "Stall Inception in a High-Speed Axial Compressor," PhD. Dissertation, University of Notre Dame, IN.
- [33] Berdanier, R. A., Smith, N. R., Young, A. M., and Key, N. L., 2018, "Effects of Tip Clearance on Stall Inception in a Multistage Compressor," *J. Propul. Power*, **34**(2), pp. 308–317.
- [34] Horwood, J. T. M., Hualca, F. P. T., Wilson, M., Scobie, J. A., Sangan, C. M., Lock, G. D., Dahlqvist, J., and Fridh, J., 2020, "Flow Instabilities in Gas Turbine Chute Seals," *ASME J. Eng. Gas Turbines Power*, **142**(2), p. 021019.